CrossMark

Causes of WRF surface energy fluxes biases in a stratocumulus region

A. Jousse[1] · A. Hall[1] · F. Sun[1] · J. Teixeira[2]

Abstract In this study, we evaluate the ability of the Weather Research and Forecasting model to simulate surface energy fluxes in the southeast Pacific stratocumulus region. A total of 18 simulations is performed for the period of October to November 2008, with various combinations of boundary layer, microphysics, and cumulus schemes. Simulated surface energy fluxes are compared to those measured during VOCALS-REx. Using a process-based model evaluation, errors in surface fluxes are attributed to errors in cloud properties. Net surface flux errors are mostly traceable to errors in cloud liquid water path (LWP_{cld}), which produce biases in downward shortwave radiation. Two mechanisms controlling LWP_{cld} are diagnosed. One involves microphysics schemes, which control LWP_{cld} through the production of raindrops. The second mechanism involves boundary layer and cumulus schemes, which control moisture available for cloud by regulating boundary layer height. In this study, we demonstrate that when parameterizations are appropriately chosen, the stratocumulus deck and the related surface energy fluxes are reasonably well represented. In the most realistic experiments, the net surface flux is underestimated by about 10 W m^{-2}. This remaining low bias is due to a systematic overestimation of the total surface cooling due to sensible and latent heat fluxes in our simulations. There does not appear to be a single physical reason for this bias. Finally, our results also suggest that inaccurate representation of boundary layer height is an important factor limiting further gains in model realism.

Keywords Stratocumulus · Surface energy fluxes · Weather Research and Forecasting (WRF) model · Physics parameterization schemes · VOCALS-REx

1 Introduction

Climatological conditions over the eastern boundary of the subtropical oceans favor the formation of persistent stratocumulus decks (Klein and Hartmann 1993). Large-scale subsidence promotes dry and stable conditions in the lower troposphere, and helps maintain a surface anticyclone and associated alongshore equatorward winds. These winds induce coastal upwelling, reducing ocean surface temperature. As a result of these relatively low sea surface temperatures and warm air aloft, the boundary layer is shallow and moist, and is often topped with a layer of stratocumulus (e.g. Garreaud and Munoz 2005). In return, these low clouds have a significant impact on the global and regional climate, due to their radiative properties. Despite their importance, stratocumulus properties are generally poorly represented in climate models (e.g. Wyant et al. 2010; Nam et al. 2012). The physical processes that drive the stratocumulus dynamics have much smaller length scale than the typical grid spacing of a regional or global model (e.g. boundary layer turbulence and cloud droplet coalescence). To represent these subgrid scale processes, climate models use parameterizations. Microphysics (MP), boundary layer (BL), and cumulus (CU) schemes are the main parameterizations affecting low cloud dynamics. However, these parameterizations lack by definition an explicit treatment of low cloud dynamics and are often sources of errors in low cloud simulations.

✉ A. Jousse
jousse@atmos.ucla.edu

[1] Department of Atmospheric and Oceanic Sciences, University of California, Los Angeles, Los Angeles, CA, USA

[2] Jet Propulsion Laboratory, California Institute of Technology, Pasadena, CA, USA

Springer

In this study, we evaluate the ability of the Weather Research and Forecasting (WRF) model to simulate stratocumuli. WRF is a community regional scale model that offers an array of MP, BL and CU schemes. WRF performance in simulating low clouds has already been evaluated in a single column model framework (e.g. Huang et al. 2013). However, only few studies have been dedicated to an inter-comparison of the various schemes in a 3D framework (e.g. Zhang et al. 2011). Moreover, the main focus in these previous studies was on low cloud properties. Here instead, our primary focus is on surface energy fluxes, essential elements of the regional climate system. Stratocumuli affect them in multiple ways (e.g. through their radiative and turbulent properties). The various processes parameterized by MP, BL and CU schemes are all potential contributors to these fluxes. However, we are not aware of any study that quantifies their relative contributions. In this work, we aim to provide that missing information. Our objectives are: (1) to examine WRF performance in representing the various components of the surface energy fluxes in a stratocumulus regime, (2) to attribute errors in surface fluxes to the respective errors in cloud properties and (3), to relate these errors to physical processes. Thus, this work is intended to be relevant to both the model user and the model developer. We aim to inform the model user whether or not WRF can realistically represent the surface fluxes in a stratocumulus region, and provide guidance as to which parameterizations to use. We aim to inform the model developer which physical processes and parameterizations are limiting model performance and to what degree.

The testbed for this investigation is the southeast Pacific in October and November 2008. This region off the coast of Peru and northern Chile is covered with the world's largest and most persistent stratocumulus deck. A major field campaign, the VAMOS Ocean-Cloud-Atmosphere-Land Regional Experiment (VOCALS-REx; Wood et al. 2010), took place during this study-period. Thus we have access to numerous in situ measurements for model evaluation purposes. In Sect. 2, we present the model set up and the parameterizations. In Sect. 3, we describe the observational data-set and the model evaluation methodology. In Sect. 4, we analyze the radiative components of the surface energy fluxes while in Sect. 5, we focus on sensible and latent heat fluxes. In Sect. 6, we focus on the net effect and we diagnose the most important mechanisms contributing to the simulated spread. Finally, in the last two sections we conclude and discuss our main findings.

2 Model setup

In this study, we use WRF model version 3.3.1 (Skamarock et al. 2008). Our model domain covers the tropical and subtropical southeast Pacific and a portion of the South American continent with two nested domains. The outer and inner domains have horizontal resolution of 45 and 15 km, respectively. In this paper, we only present results from the innermost domain, shown in Fig. 1 (The results for the outer-most domain are quantitatively consistent with those for innermost domain). There are 43 sigma-levels in the vertical, with enhanced resolution near the lower boundary (30 sigma-levels below 700 hPa). The model is initialized on 2 October 2008, and run continuously for 60 days. The initial and lateral boundary conditions for the WRF model simulations are derived from the National Centers for Environmental Prediction's final analysis field (FNL) at $1° \times 1°$ horizontal resolution every 6 h. The sea surface temperature prescribed at the lower boundary is provided by continuous daily-varying optimum interpolation sea surface temperature analysis (Reynolds and Smith 1994). The model output is stored every 3 h. To ensure smooth solutions, the domain grid cells closer than 5 cells from the boundary are relaxed towards the FNL solution.

WRF provides numerous parameterization options apart from MP, BL and CU schemes. In this study, our choices are: Rapid Radiative Transfer Model (RRTM) long wave radiation (Mlawer et al. 1997); Dudhia (1989) shortwave radiation schemes; and the NOAH Land Surface Model (Chen and Dudhia 2001) for land surface processes including vegetation, soil, snowpack and land atmosphere energy, momentum and moisture exchange.

The physical processes governing low cloud dynamics are primarily parameterized in WRF with BL, MP and CU schemes. In this study, we test the sensitivity to these schemes by performing a total of 18 runs (See Table 1 for a list of the tested schemes with references and the "Appendix" for more details). Three MP (Lin, WSM6, Thompson) and five BL (YSU, ACM2, MYJ, MYNN, QNSE) schemes are cross-tested while using the KF cumulus scheme (no shallow cumulus parameterization). One additional run is performed using the MYNN BL scheme, with the droplet concentration tuned to 100 cm^{-3} instead of 300 cm^{-3} in WSM6 (These two values correspond to the observed range during VOCALS-REx; e.g. Bretherton et al. 2010). To study the effect of a cumulus scheme that includes a shallow cumulus parameterization, we perform two additional experiments with Tiedtke and the BL schemes MYNN and YSU while using WSM6 as the MP scheme (See Table 2 for our matrix of experiments). The schemes tested use a variety of methodologies and formulations and thus, our suite of experiments can be considered broadly representative of WRF performance.

Note that we did some additional tests using the CU scheme Tiedtke with the shallow cumulus parameterization switched off (i.e. only deep convection on). The results are very similar to those with KF. Thus, the differences

between KF and Tiedtke (when the shallow CU is on) can be attributed to the shallow cumulus parameterization in Tiedtke. To avoid redundant information we will only show the experiments that use Tiedtke with the shallow CU switched on.

Surface heat and moisture fluxes are handled by the surface layer scheme. We use the Monin–Obukhov scheme (Beljaars 1994) for the runs using the BL schemes YSU, MYNN and ACM2. QNSE and MYJ are not compatible with the Monin–Obukhov scheme so we use instead the QNSE surface layer scheme for QNSE and the Monin–Obukhov Janjic Eta scheme (Janjic 1994) for MYJ. MYNN is also compatible with the Monin–Obukhov Janjic Eta scheme and the MYNN surface layer scheme, and we did some additional tests using those. However, the effects of these various surface layer schemes on our results are negligible. Therefore, in our analysis differences between simulations will not be attributed to the surface layer schemes.

3 Observations and data processing

3.1 VOCALS-REx dataset

In this work we use the VOCALS-REx data collected on the Ronald Brown vessel from October 25 to November 29 2008 (N.B., no data are available on November 3–10) along the 20°S transect between 86°W and 72°W (de Szoeke et al. 2010). We take advantage of the various surface data (e.g. latent and sensible heat fluxes), vertical profiles (e.g. temperature and specific humidity), as well as cloud related variables (e.g. cloud top height and liquid water path) measured during that campaign to evaluate the model's performance.

3.2 Remote sensing dataset

We also use cloud cover (CC) and liquid water path (LWP) measured by the Moderate-resolution Imaging Spectrometer (MODIS, Platnick et al. 2003; Platnick 2007). MODIS is deployed on 2 polar-orbiting satellites, Aqua and Terra, which pass over the equator twice a day at 1:30 and 10:30 a.m./p.m. local time, respectively (LWP data are only available during daytime at 10:30 a. m. and 1:30 p.m.). MODIS data allow a comparison over the entire southeast Pacific, as MODIS scans cover 90 % of this region, on average. In this study, we correct MODIS LWP data according to the adiabatic liquid water profile assumption, as it is the most realistic in the Southeast Pacific (i.e. we multiply MODIS LWP data by 0.83; e.g. Borg and Bennartz 2007). Our comparison with in situ measurements reveals that MODIS LWP data overestimate in situ measurements in the southeast Pacific by about 15 % (not shown; similar results are

seen in Painemal and Zuidema 2011). However, these uncertainties do not affect our conclusions, as the model spread is much greater than observational uncertainties.

3.3 Data processing

To ensure the comparison between model data and observations is well posed, we process them both. When compared to MODIS, we select the same phase of the observed diurnal cycle in simulations by linearly interpolating WRF 3-hourly outputs onto the satellite measurements times. When compared to VOCALS-REx measurements, we select the model grid points nearest to the locations measured during this field campaign. VOCALS-REx observations are taken every 10 min, and to select the same phase of simulated diurnal cycle, we average the 6 measurements closest in time to each 3-hourly snapshot in the model output. As CC was >85 % during VOCALS-REx, this data set is well suited to evaluate the representation of the stratocumulus regime in WRF. Moreover, for the quantities examined, averages over the nearest grid points measured during VOCALS-REx are well correlated ($r > 0.9$) to averages over the grid cells along the 20°S transect between 86°W and 72°W during October and November 2008. Therefore, the general conclusions we reach are not dependent on the limited sample of measurements.

The resolution mismatch between model and in situ measurements is potentially an issue as we compare 15-km grid cells to point measurements. However, we compare a given model grid cell with the average across 6 point-measurements that sample sub-grid variability, suppressing such biases. We also include error bars that represent observational standard deviations to account for potential biases due to the scale mismatch in the comparison.

There is no CC parameterization in WRF, so we define simulated CC to be 100 % if a grid cell has a LWP >5 g m^{-2} (CC is set to 0 otherwise). Although simple, this definition is appropriate as 5 g m^{-2} roughly corresponds to the minimum LWP that satellite instruments can detect (e.g. MODIS). Since it is not well posed to compare CC using this binary definition computed on a 15-km model grid to point measurements, we use MODIS CC as the observational data set. To account for the resolution mismatch between the model and MODIS (15 vs. 1–5-km), we interpolate MODIS level 2 data (i.e. orbital swath) to the same grid as WRF. Then, to match our definition of CC in the model as well as possible, we set interpolated MODIS 15-km pixels with CC >0 as 100 % cloudy. We call this variable the upper bound for MODIS 15-km CC. We also define a lower bound for MODIS 15-km CC. In this case, only the MODIS 15-km pixels with CC >50 % are defined as 100 % cloudy, while others are set as non-cloudy.

Table 1 List of BL, MP and CU schemes tested in this study

	Boundary Layer (BL) schemes	
YSU (Y)	The Yonsei University scheme is a first order closure (Hong et al., 2006). YSU explicitly represents non-local mixing and entrainment.	
ACM2 (A)	The Asymmetric Convective Model version 2 is a first order closure (Pleim, 2007). ACM2 has a representation for non-local mixing.	
MYJ (J)	The Mellor Yamada Janjic scheme is turbulent kinetic energy based (Janjic, 1990).	
MYNN (N)	The Mellor Yamada Nakanishi and Niino scheme is turbulent kinetic energy based (Nakanishi and Niino, 2004).	
QNSE (Q)	The Quasi-normal scale elimination scheme is turbulent kinetic energy based (Sukoriansky et al., 2005).	
	Microphysics (MP) schemes	
Lin (•)	The Lin scheme is a single moment 6-class scheme (Lin et al, 1983).	
WSM6 (•)	WSM6 is the WRF Single Moment 6-class scheme (Hong et al., 2003). It has a tunable critical droplet number concentration (set by default to 300 cm^{-3}).	
Thompson (•)	Thompson is a double moment scheme (Thompson et al., 2008). It has a tunable critical droplet number concentration (set by default to 100 cm^{-3}).	
	Cumulus (CU) schemes	
KF	The Kain and Fritsch scheme only parameterizes deep convection (Kain and Fritsch, 1990).	
Tiedtke (t)	The Tiedtke scheme parameterizes both shallow and deep convective plumes (Zhang et al., 2011)	

See "Appendix" for details

Table 2 Matrix of experiments with MP schemes on the left and BL and CU schemes on the top

	ACM2 KF	MYJ KF	MYNN KF	QNSE KF	YSU KF	MYNN Tiedtke	YSU Tiedtke
Lin	**A**	**J**	**N**	**Q**	**Y**		
Thompson N$_c$=100 cm-3	A	J	N	Q	Y		
WSM6, N$_c$=300 cm-3	Y	J	N	Q	Y	Nt	Yt
WSM6 N$_c$=100 cm-3			N				

Simulated CC is considered realistic if it falls within these two extremes.

In this study, we use two distinct variables for LWP: (1) the cloud LWP (LWP$_{cld}$) corresponding to the average LWP over grid cells or point measurements considered cloudy (i.e. those with LWP >5 g m^{-2}), and (2) the total LWP (LWP$_{tot}$), which does not discriminate between cloudy and non-cloudy grid cells. This distinction allows to differentiate contributions due to the integrated liquid water in clouds from those related to cloud frequency (i.e. cloud cover). However, the resolution mismatch between point measurements and WRF necessarily produces systematic overestimates in measurements of LWP$_{cld}$ on a 15-km grid. We estimate a correction factor of 5 % by using MODIS level 2 CC data. This correction factor is relatively small compared to LWP uncertainties already included in our errorbars. Therefore its impact on our analysis is minimal.

For model and observations, grid points with cloud top temperature lower than 270 K are set to zero CC to ensure we are examining only low cloud. This is a reasonable threshold for low clouds in the southeast Pacific. Since MODIS cloud top pressures are not accurate for low clouds (Marchand et al. 2010), we use this temperature threshold instead. In any case, higher clouds with cloud top temperature below 270 K represent <5 % of the cloudy events in both model and observations during our study period. Thus, the chosen criteria for low cloud has a negligible impact on our results, no matter how arbitrary it may be.

3.4 Satellite-based model evaluation

Cloud cover (CC) and liquid water path (LWP) are two natural variables to characterize a cloud field. We show in Fig. 1a unprocessed MODIS mean cloud cover (colors) as well as MODIS mean LWP$_{cld}$ (contours; LWP$_{cld}$ referring to cloudy pixels only; see Sect. 3.3 for details) during October and November 2008 over the Southeast Pacific. This figure confirms the existence of a stratocumulus deck that covers 80 % of the region on average, and peaks about 500 km offshore. LWP$_{cld}$ increases away from the coast, in accordance with the observed deepening of the boundary layer (e.g. Rahn and Garreaud 2010a). MODIS unprocessed CC in Fig. 1a is very similar to what we define as the lower bound for MODIS 15-km CC (not shown; see Sect. 3.3 for details on MODIS 15-km CC). In Fig. 1b, we show the corresponding upper bound for MODIS 15-km
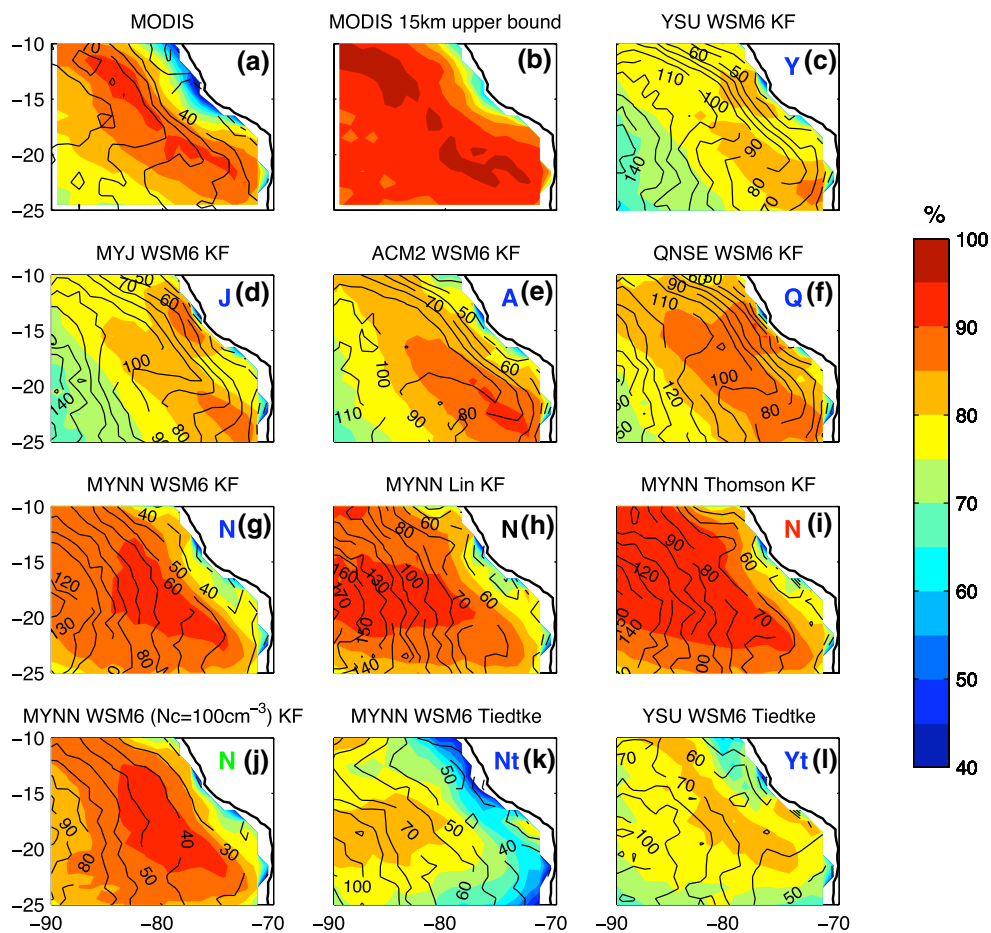
Fig. 1 a MODIS low cloud cover (*shaded*, %), and MODIS LWP$_{cld}$ (low cloud events only, contour, g m^{-2}); **b** upper bound for MODIS 15-km low CC (%, see text for details); WRF 15-km low cloud cover (*shaded*, %) and LWP$_{cld}$ (low cloud events only, contour, g m^{-2}) using the MP scheme WSM6, the CU scheme KF, and the BL scheme YSU (**c**), MYJ (**d**), ACM2 (**e**), QNSE (**f**), MYNN (**g**); **h** As in **g** but using the MP Lin; **i** As in **g** but using the MP Thompson; **j** As in **g** but using WSM6 with a droplet concentration of 100 cm^{-3}; **k** As in **g** but using the CU scheme Tiedtke; **k** As in **c** but using the CU scheme Tiedtke. The corresponding data are averaged over October/November 2008. Cloud cover data are averaged between Aqua and Terra overpasses (1:30 and 10:30 a.m./p.m. LT). LWP$_{cld}$ data are averaged between Aqua and Terra daytime overpasses (1:30 p.m. and 10:30 a.m. LT). *Capital letters* on the upper right of each figure correspond to the representation used for the respective experiments in the remaining figures of this paper

CC. It is much more homogeneous than MODIS unprocessed CC, with values >90 % over most of the domain. In the remaining panels of Fig. 1, we plot the simulated CC and LWP$_{cld}$ for a representative sample of our simulations. A stratocumulus deck can clearly be identified in all experiments. Overall, the simulated CC falls within the observational range or is slightly lower than the lower bound. Our simulations also capture the offshore increase of LWP$_{cld}$.

4 Surface radiation fluxes

We now discuss the relationships between cloud properties and surface radiation fluxes. To discuss the differences across our experiments more quantitatively, we focus on

domain averages over the nearest grid cells measured during VOCALS-REx (see Sect. 3.3 for details).

The scatterplot in Fig. 2a illustrates the positive correlation between CC and downward longwave radiation flux at surface (LW; r = 0.81). The relationship between CC and LW arises from the fact that CC is the primary means by which clouds influence the greenhouse effect. Observations stand very close to the regression line relating these two variables. This gives confidence that if the model were to simulate the correct CC, it would produce realistic LW. In other words, model errors in LW are probably not attributable to problems with the radiative transfer subroutine.

During VOCALS-REx, the CC range across our experiments is relatively small, between 80 and 90 %. The MODIS 15-km lower bound for the corresponding grid
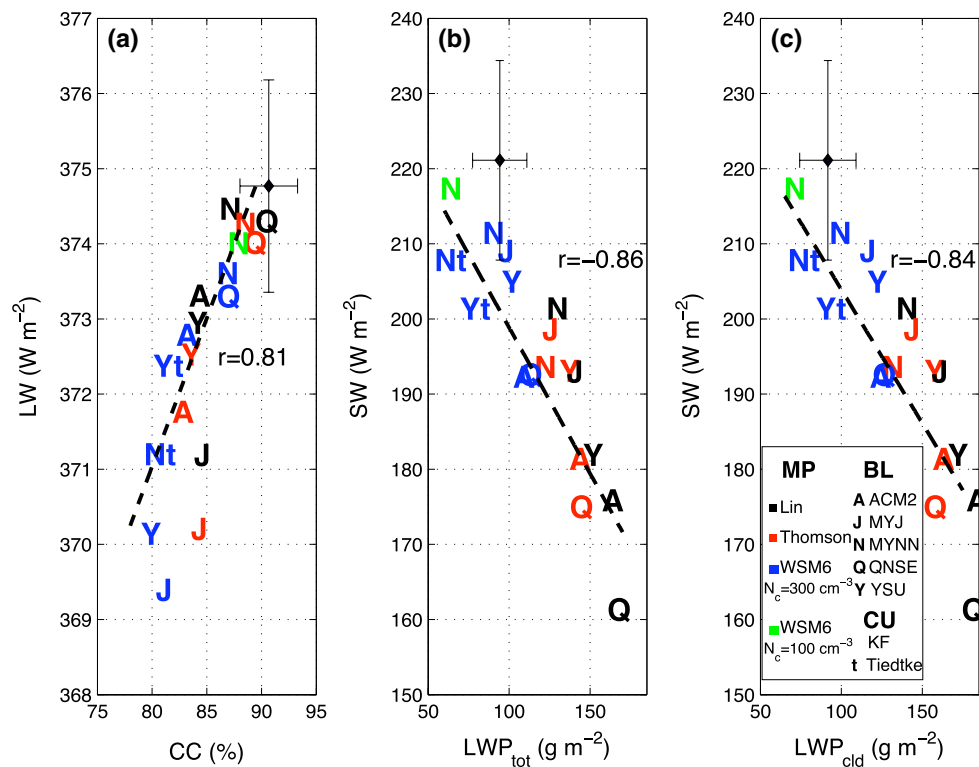
Fig. 2 a Downward surface longwave flux (W m^{-2}) as a function of CC; **b** downward surface shortwave flux (W m^{-2}) as a function of LWP$_{tot}$ (g m^{-2}); **c** downward surface shortwave flux (W m^{-2}) as a function of LWP$_{cld}$ (g m^{-2}). Data are averaged over grid cells measured during VOCALS-REx from October 25 to November 29 along the 20°S transect. The *black diamond* corresponds to VOCALS-REx measurements on the Ron Brown vessel (except for CC in *panel a*, which corresponds to MODIS data). *Error bars* that account for potential biases due to the comparison methodology are also included (see Sect. 3.3). The *dashed lines* represent the least squares regression between simulated variables

points is 88 %, so that the model generally slightly underestimates CC, consistent with Fig. 1. Figure 2a also shows that BL scheme is the primary control on CC. In fact, the CC range associated with the various MP schemes is <3 %, while it is more than 10 % for the BL schemes. The CU scheme also contributes to the spread in CC. In fact, when the CU scheme Tiedtke is used instead of KF, CC is reduced by about 7 % in the test with MYYN. However, this reduction is not systematic as there is no significant change when Tiedtke is combined with YSU. The best results for CC are realized when the CU scheme KF (which has no shallow cumulus parameterization) is combined with MYNN or QNSE. In that case simulated LW (~375 W m^{-2}) is within observational error. In the least realistic simulation (with MYJ), the lower observational bound for LW (~373 W m^{-2}) is underestimated by about 5 W m^{-2}. This is much smaller than other surface energy biases discussed below. Thus, CC errors may not be that consequential for LW, and our simulations can be considered fairly realistic for this component of the surface energy flux.

Turning to the downward shortwave flux at surface (SW), Fig. 2b reveals a strong anti-correlation between SW and the total liquid water path (LWP$_{tot}$) in the model (r = −0.86). This relationship is the result of the fact that LWP$_{tot}$ controls optical depth in stratocumuli (e.g. Borg and Bennartz 2007). For VOCALS-REx grid cells, the relationship between SW and the cloud liquid water path (LWP$_{cld}$) is as strong as the one with LWP$_{tot}$ (r = −0.84; Fig. 2c). Apparently CC variations do not contribute strongly to variations in SW. This may be because the simulated spread in CC is relatively small (Fig. 2a). To focus on the most important processes for SW, we center our discussion on LWP$_{cld}$.

As with CC and LW, observations stand very close to the regression line that relates SW and LWP$_{cld}$ in the simulations. This gives confidence that if the model were to simulate the correct LWP$_{cld}$, it would produce realistic SW fluxes. As with LW, this also implies model errors in SW are probably not attributable to problems with the radiative transfer subroutine. Simulated LWP$_{cld}$ generally overestimates observations and as a result, most experiments

Fig. 3 **a** Surface sensible heat flux (W m^{-2}); **b** surface latent heat flux (W m^{-2}); **c** average BL liquid potential temperature (K); and **d** average BL total specific humidity as a function of BL height (m). Data are averaged over grid cells measured during VOCALS-REx from October 25 to November 29 along the 20°S transect. The *black diamond* corresponds to VOCALS-REx measurements on the Ron Brown vessel. *Error bars* that account for potential biases due to the comparison methodology are also included (see Sect. 3.3). The *dashed lines* represent the least squares regression between variables
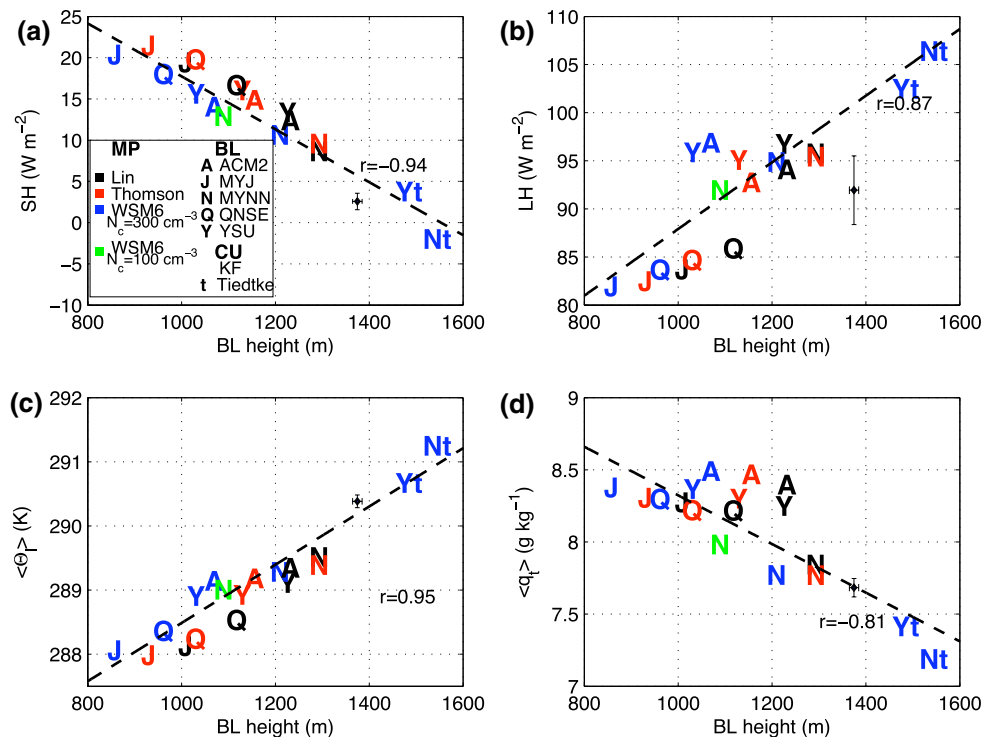
underestimate SW. The simulated range goes from 160 to 220 W m^{-2} for SW and from 60 to 180 g m^{-2} for LWP, while observations stand close to 218 W m^{-2} ($\pm$15 W m^{-2}) and 91 g m^{-2} ($\pm$15 g m^{-2}).

MP, BL and CU schemes all contribute to the spread in LWP$_{cld}$ and SW. However, the MP contributions are the greatest. Experiments using Thompson and Lin systematically underestimate the observed lower bound for SW by 5–45 W m^{-2} and overestimate the LWP$_{cld}$ upper bound by 20–70 g m^{-2}. The biases are reduced to <15 W m^{-2} for SW and 10 g m^{-2} when WSM6 is used instead. For a given MP scheme, and when the CU scheme is fixed to KF, results are best when the BL scheme MYNN is used. When both MYNN and WSM6 are employed with N$_c$ = 300 cm^{-3}, simulated SW and LWP are within the uncertainty range. When the CU scheme KF is replaced by Tiedtke in the tests that use the BL schemes YSU and MYNN with the MP scheme WSM6, LWP$_{cld}$ is reduced by about 25 g m^{-2} and SW is very close or within the observed uncertainty range. Thus, MP, BL and CU schemes all contribute in multiple ways to SW and LWP$_{cld}$. The mechanisms that control LWP$_{cld}$ will be analyzed in Sect. 6.

5 Sensible and latent heat fluxes

In this section, we focus on sensible heat (SH) and latent heat (LH) fluxes. It turns out that the boundary layer variable most tightly linked to both is BL height. To determine BL height, we follow the same methodology as Rahn and Garreaud (2010b) (Note that average BL height matches cloud top height almost perfectly in both model and observations. Thus, we can use these two terms interchangeably without ambiguity).

In Fig. 3a, b, we show that SH and LH are significantly correlated to BL height (r = -0.94 and r = 0.87, respectively). To diagnose the potential contributors to these relationships, we scatter BL height against average BL liquid potential temperature ($\langle \Theta_l \rangle$; Fig. 3c) and average BL total specific humidity ($\langle q_t \rangle$; Fig. 3d). These figures show that simulations with greater BL heights have systematically greater $\langle \Theta_l \rangle$ (r = 0.95) and smaller $\langle q_t \rangle$ (r = -0.81). Such relationships are consistent with the fact that higher boundary layers entrain warmer and drier air into the BL, which controls $\langle \Theta_l \rangle$ and $\langle q_t \rangle$ from the BL top. Apparently, this mechanism controls temperature and specific humidity all the way to the surface, as surface air temperature and surface specific humidity exhibit nearly identical relationships with BL height (not shown). In our experiments, SH and LH decrease with surface air temperature (r = -0.94; not shown) and surface specific humidity (r = -0.70; not shown), respectively (Note that since sea surface temperature is forced in our experiments, it does not contribute to the spread in SH and LH). Thus, this suggests that BL height likely contributes to SH and LH in our simulations. However, feedbacks processes are also likely, since SH and

LH are potential drivers of the BL deepening. As a result, the relationships exhibited in Fig. 3a, b are most likely the result of interconnections between SH, LH and BL height. Observational values are fairly close to the regression lines that relate simulated BL heights to SH, LH, $\langle \Theta_l \rangle$ and $\langle q_t \rangle$. This once again gives confidence that if the model were to produce realistic BL height, SH and LH would also be fairly realistic.

The average BL height observed during VOCALS-REx is 1380 m, while it ranges from 900 to almost 1600 m in our simulations (Note that the observed offshore increase in BL height is well captured in all the simulations; not shown). BL and CU schemes are the main contributors to the BL height spread across our experiments, although MP contributions are not negligible (± 150 m for a given BL scheme). When the CU scheme KF is used (i.e. no shallow CU parameterization), the simulated BL is systematically underestimated. The most realistic BL heights are simulated with MYNN. In that case, BL heights are underestimated by <150 m when combined with WSM6, and by <50 m when combined with Lin or Thompson. The shallow cumulus parameterization in Tiedtke promotes the deepening of the BL. However, this deepening is too pronounced as BL height is overestimated by more than 150 m in our two tests. Thus, none of our simulations matches the observed BL height precisely, though some come close.

As a result of the BL height underestimation for the experiments using the cumulus scheme KF, temperature in the BL is generally colder than observed (between 288 and 289.5 K instead of 290.5 K; Fig. 3c), and SH is often overestimated (between 22 and 9 W m^{-2} instead of 2 W m^{-2}; Fig. 3a). MYNN behaves the best with a cold bias of about 1 K and an overestimation of SH by almost 10 W m^{-2}. When the CU Tiedtke is combined with MYNN, the BL temperature has a warm bias of about 1 K and SH is underestimated by almost 10 W m^{-2}. When Tiedtke is combined with YSU, $\langle \Theta_l \rangle$ and SH almost match observations (biases are <0.3 K and <2 W m^{-2}, respectively). Similarly, BL specific humidity is moister than observed when KF is used (between 8.5 and 7.8 g kg^{-1} instead of 7.7 g kg^{-1}), with MYNN being the closest. When the cumulus scheme Tiedtke is used instead of KF, the BL is too dry, with low biases of 0.2 and 0.4 g kg^{-1} in the cases of YSU and MYNN, respectively. For LH, all the simulations that use ACM2, YSU and MYNN (with KF) are within the observed uncertainty range (92 $\pm$ 6 W m^{-2}), while those that use QNSE and MYJ underestimate LH by almost 10 W m^{-2}. LH is overestimated by about 10 W m^{-2} in the two simulations that use the CU scheme Tiedtke.

None of our experiments perfectly represents both SH and LH. There are also systematic compensations between SH and LH in the model. In fact, their rates of change
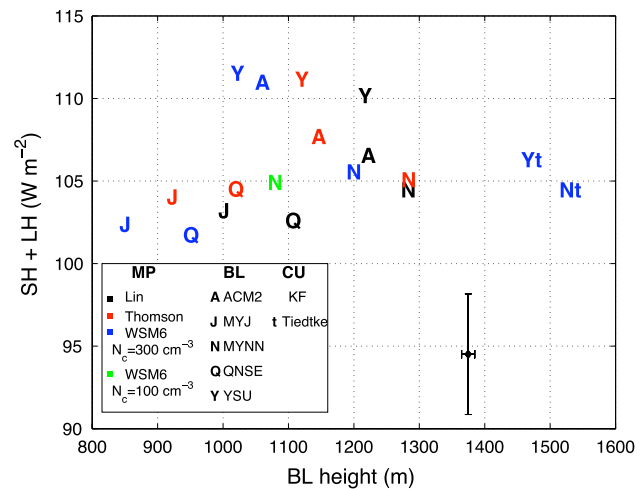
Fig. 4 As in Fig. 3, but with the sum of LH and SH on the y-axis (W m^{-2})

with BL height have similar amplitudes (~0.03 W m^{-2} per meter) but opposite signs. As a result, the total cooling contribution to the surface energy budget from LH and SH is nearly constant. It is close to 107 W m^{-2} in all our simulations (see Fig. 4). As the observed upper bound is close to 98 W m^{-2}, the model systematically overestimates the total cooling of the surface from LH and SH by about 10 W m^{-2}. However, there does not appear to be a single physical reason for this.

6 Net surface flux

To underline the implications of cloud biases for surface energy balance, we now focus on the net surface energy flux. We first look at its radiation component in Fig. 5a. Downwelling SW and LW both contribute positively to the net radiation surface flux, while the outgoing longwave radiation contributes negatively to it (Note that we account of a sea surface albedo of 0.05 to compute the net shortwave flux at surface in both model and observations). As the sea surface temperatures prescribed in our experiments agree well with observed values during the Ron Brown field measurement, the simulated outgoing longwave radiation at the surface matches observations, with an average value of 397 W m^{-2} during VOCALS-REx. The net radiation flux at surface is highly correlated (r = $-$0.86) to LWP$_{cld}$. This is consistent with results shown in Fig. 2. Thus SW, primarily controlled by LWP$_{cld}$, dominates the spread in the radiation component of the energy flux. As with SW and LW, the regression line is within observational uncertainties. This once again gives confidence that if the model were to produce realistic LWP$_{cld}$, it would produce a realistic net surface radiation flux.
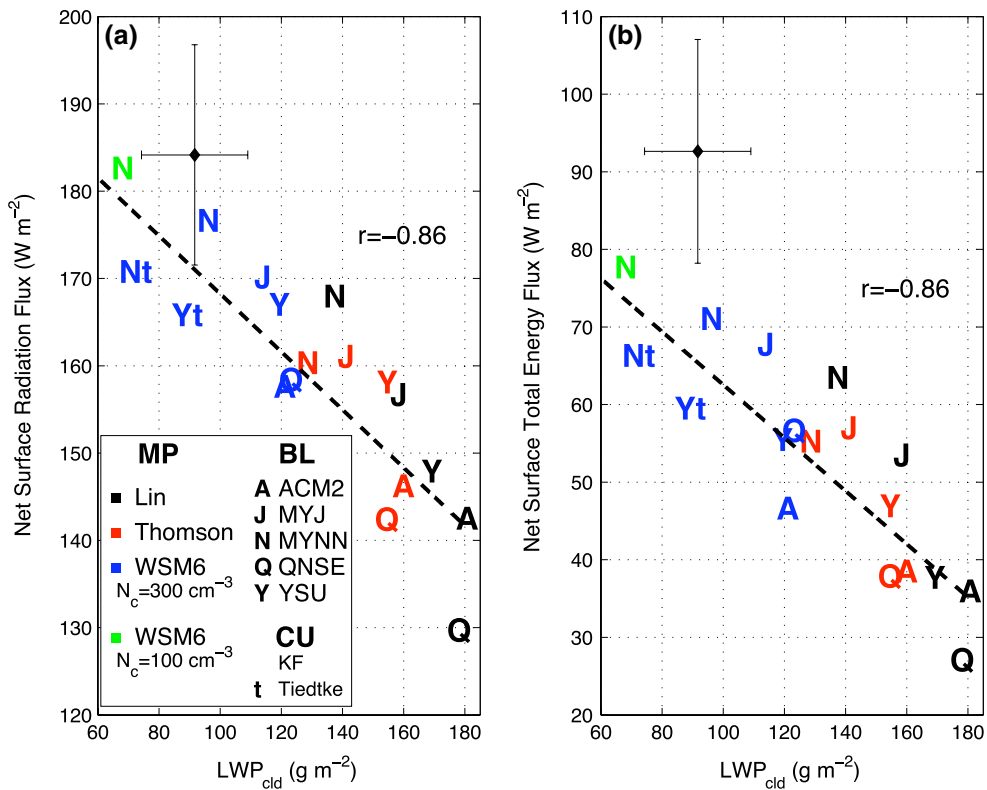
Fig. 5 **a** Net surface radiation flux (W m^{-2}), and **b** net surface total energy flux (W m^{-2}) as a function of LWP$_{cld}$ (g m^{-2}). Data are averaged over grid cells measured during VOCALS-REx from October 25 to November 29 along the 20°S transect. The *black diamond* corresponds to VOCALS-REx measurements on the Ron Brown vessel. *Error bars* that account for potential biases due to the comparison methodology are also included (see Sect. 3.3). The *dashed lines* represent the least squares regression between variables

Fig. 6 LWP$_{cld}$ (g m^{-2}) as a function of the average BL total specific humidity ($\langle q_t \rangle$, g kg^{-1}). The *dashed lines* represent the least squares regression between variables for a given MP scheme (*blue for WSM6, red for Thompson, and black for Lin*). Data are averaged over grid cells measured during VOCALS-REx from October 25 to November 29 along the 20°S transect. The *black diamond* corresponds to VOCALS-REx measurements on the Ron Brown vessel. *Error bars* that account for potential biases due to the comparison methodology are also included (see Sect. 3.3)
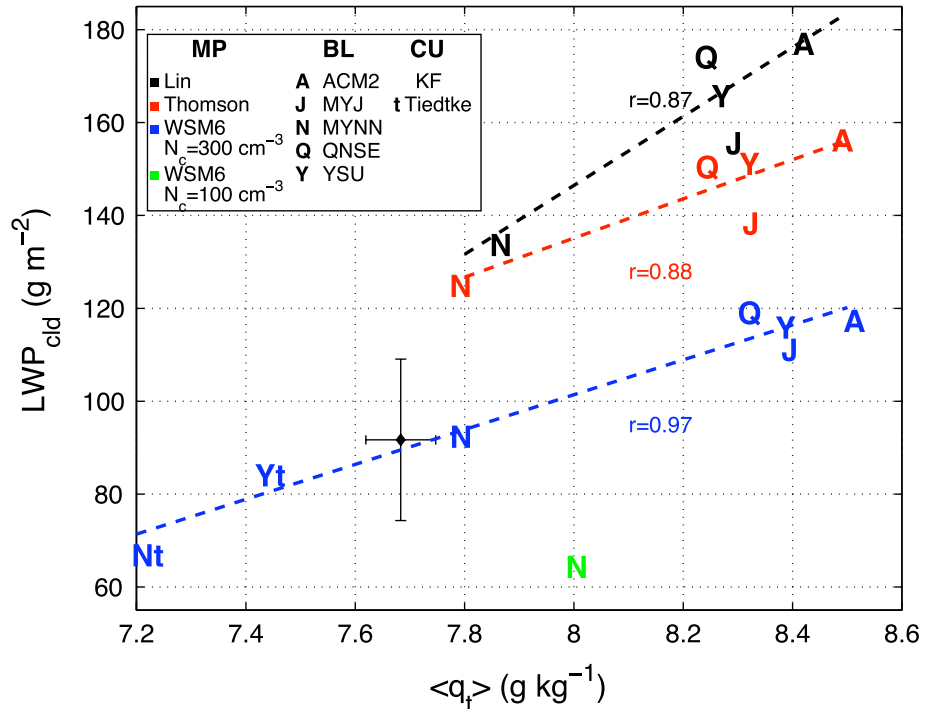
In Fig. 5b, we turn to the net surface energy flux. To compute this flux, latent and sensible heat fluxes are subtracted from the net radiation flux. The relationship between LWP_{cld} and the net energy flux ($r = -0.86$) is very similar to the relationship between LWP_{cld} and the net radiation flux. The variations in the net radiation flux seem to control the variations in the net energy flux. As shown in Fig. 4, the sum of LH and SH is roughly constant in our experiments. Thus, it does not contribute to the spread of the net surface energy flux. However, the sum of LH and SH is systematically overestimated by about 10 W m^{-2}. This explains why the few simulations with realistic LWP$_{cld}$ underestimate the lower bound of the net surface flux by about 10 W m^{-2} (e.g. in the experiment that combined MYNN, KF and WSM6).

Removing the approximate 10 W m^{-2} bias in the sum of LH and SH still leaves an underestimation of the observed net surface flux (93 ± 15 W m^{-2}) in many of the simulations. This is due to an overestimation of LWP_{cld}, and too little incoming solar radiation (Fig. 2b). To investigate the reasons for this, we scatter LWP_{cld} against average BL specific humidity in Fig. 6. This figure shows that for a given MP scheme, LWP_{cld} increases at a rate close to 40 g m^{-2} per g kg^{-1} of $\langle q_t \rangle$ as BL schemes are swapped out. The case of WSM6, where 7 experiments have been carried out, is a good support for the robustness of this relationship ($r = 0.97$). Figure 5b also shows that, for any BL scheme, LWP_{cld} changes by roughly a constant value from one MP scheme to another, while $\langle q_t \rangle$ remains almost unchanged. For example, when Thompson replaces WSM6, LWP_{cld} increases by about 40 g m^{-2}. Note that Lin behaves slightly differently as LWP_{cld} increases with a greater rate of $\langle q_t \rangle$ than the other two MP schemes (65 vs. 40 g m^{-2} per g kg^{-1} of $\langle q_t \rangle$). Nevertheless, the behavior of Lin remains similar and does not undermine our argumentation.

The data in Fig. 6 indicate that two mechanisms are potentially controlling LWP_{cld}. The first involves BL and CU schemes. These schemes determine BL depth and BL specific humidity (see Sect. 4). The BL specific humidity, in turn, limits the liquid water supply to the cloud, and thus LWP_{cld}. The second mechanism involves MP schemes, which systematically change LWP_{cld} independently of $\langle q_t \rangle$. MP schemes simulating higher LWP_{cld} consistently produce less precipitation (not shown). Thus, MP schemes contribute to LWP_{cld} through the formation of raindrops. Note that BL and MP contributions to LWP_{cld} cannot clearly be identified when each simulation is analyzed individually. Thus, our multi-simulations approach enables the identification of processes contributing to LWP_{cld} that were otherwise not straightforward to untangle. According to Fig. 6, microphysical and specific humidity contributions to LWP_{cld} are most realistic when WSM6 is combined with MYNN and KF, as well as with YSU and Tiedtke.

However, the representation of the specific humidity contribution remains slightly unrealistic as $\langle q_t \rangle$ is overestimated and underestimated by about 1 g kg^{-1} and 2 g kg^{-1}, respectively. As mentioned in Sect. 4, $\langle q_t \rangle$ biases are related to biases in BL heights.

The two experiments that use WSM6 with different droplet concentration numbers highlight that the cloud droplet auto-conversion into raindrops participates in the MP contribution to LWP_{cld}. In fact, LWP_{cld} is lower in the case that favors rain formation through auto-conversion (i.e. smaller N_c) [Note that since the simulated spread in precipitation during VOCALS-REx (~0.1 mm day^{-1}) is within observed uncertainties, precipitation measurements cannot be used to determine which simulation is most realistic]. Figure 6 also suggests that a droplet concentration number of 300 cm^{-3} in WSM6 represents the microphysical contribution to LWP_{cld} better than 100 cm^{-3}. In fact, the observed lower bound for LWP is underestimated by about 6 g m^{-2} in the test that uses MYNN, KF and WSM6 with $N_c = 100$ cm^{-3}, while average LWP is realistic when $N_c = 300$ cm^{-3}. However, a closer look at the spatial pattern for LWP_{cld} in these two simulations (Fig. 1g, j) gives a more nuanced view. In fact, experiments with $N_c = 300$ cm^{-3} only matches observations in coastal regions, while the one using $N_c = 100$ cm^{-3} agrees with observations further offshore. This is consistent with the observed spatial variability for N_c, which generally reaches 300 cm^{-3} close to the coast and drops below 100 cm^{-3} 1000 km offshore (Bretherton et al. 2010). Thus, LWP_{cld} matches observations (Fig. 1a, contours) in regions where the imposed value for N_c is reasonable, providing evidence for the realism of the auto-conversion scheme in WSM6. However, due to the large spatial variability of N_c, a constant value in the model is not sufficient to represent LWP_{cld} over the entire domain. Nevertheless, for the VOCALS-REx grid points, N_c is not as critical as other factors mentioned, as differences in the net flux are <10 W m^{-2} (Fig. 5b) when it varies from 300 to 100 cm^{-3} in WSM6.

7 Conclusions

In this study, we use VOCALS-REx data and a process-based model evaluation to analyze the ability of WRF to represent surface energy fluxes in the southeast Pacific stratocumulus region. Five BL (YSU, ACM2, MYJ, MYNN, QNSE) and three MP (Lin, WSM6, Thompson) schemes are cross-tested with the CU scheme fixed to Kain-Fritsch (no shallow CU parameterization). Three additional tests with the BL scheme MYNN and the MP scheme WSM6 are also carried out: one where the droplet concentration number is tuned from 300 to 100 cm^{-3} in WSM6, and two using the CU scheme Tiedtke, which has a shallow CU

parameterization. In this last section, we summarize our main findings.

Model errors in LW and SW are not attributable to the radiative transfer subroutine. Instead, they are related to misrepresentations of cloud properties. In the case of LW, errors are primarily controlled by errors in CC. However, the average amount of low clouds is fairly realistic in all our experiments and LW errors are negligible. For SW, biases are primarily controlled by biases in LWP_{cld}. Most simulations significantly overestimate LWP_{cld} leading to underestimation of SW (60 W m^{-2} in the worst case).

Model errors in SH and LH correlate with errors in BL height. Our results suggest that the level of entrainment likely regulates SH and LH by controlling temperature and humidity at the surface. Nevertheless, feedback processes are also likely, as SH and LH are potential contributors to BL depth. Some experiments exhibit significant biases in BL height, which are associated with SH and LH biases. However, there are systematic compensating effects between these fluxes. In fact, the total surface cooling from SH and LH is close to constant in all our experiments and overestimates observations by roughly 10 W m^{-2}. There does not appear to be a single physical reason for this. However, this bias is not the primary source of errors for the net surface flux as it is negligible in comparison to the SW underestimation in most simulations. Thus, errors in net surface energy fluxes are mostly traceable to errors in LWP_{cld}, which control SW.

Given the importance of LWP_{cld} for the net surface flux, we diagnose two mechanisms that control the variability in LWP_{cld} across our experiments. One involves MP schemes, which contribute to LWP_{cld} through the production of raindrops. The second mechanism involves BL and CU schemes, which control moisture available for cloud through regulation of BL depth. By evaluating the representation of these two processes in our experiments, we attribute errors in LWP_{cld} to the schemes involved. By using a process-based evaluation, we also ensure that realistic simulation of LWP_{cld} does not take place through a compensation of errors.

According to our set of experiments, the microphysical contribution to LWP_{cld} is most accurate when the MP scheme WSM6 is used, while it is overestimated in Lin and Thompson. Our study also suggests that there is a better agreement between observed and simulated LWP_{cld} when the cloud droplet concentration number (N_c) is tuned to a realistic value in WSM6. This highlights the importance of the cloud droplet auto-conversion into raindrops for the accurate representation of LWP_{cld}. However, since the observed spatial variability for N_c is high over the region, the single value for N_c currently prescribed in the model is not appropriate to represent the spatial variability in LWP_{cld}. This will be further analyzed in a future study.

According to our pool of experiments, the specific humidity contribution to LWP_{cld} is most accurate when MYNN and KF, or YSU and Tiedtke are combined. This can be attributed to a better representation of BL depth in these two cases. However, BL heights remain slightly biased even in our two most accurate simulations. In fact, BL heights is underestimated by about 150 m when WSM6, MYNN and KF are combined, while it is overestimated by roughly the same amount in the case of WSM6, YSU and Tiedtke. These relatively small errors in BL height do not lead to noticeable biases for LWP_{cld} in these cases. Thus, the remaining net surface flux biases (~10 W m^{-2}) are primarily related to the systematic overestimation of the total cooling from LH and SH. Nevertheless, a more accurate representation of BL height would certainly help the model to gain further realism. In particular, our study suggests that BL temperature and specific humidity biases would be reduced if the BL height representation were more realistic.

8 Discussion

Our results suggest that inaccurate representation of BL height is an important factor limiting further gains in the realism of WRF. Our study suggests some possible pathways that could be investigated to improve the representation of BL height. In the following paragraphs, we discuss a few of them.

Our results show that, when no shallow cumulus parameterization is employed, WRF underestimates BL height during VOCALS-REx. Nevertheless, the behavior of MYNN is very close to reality. This could suggest that only minor modifications to MYNN might be sufficient to approach observations further. For instance, the differences between MYNN and MYJ highlight the impact of the mixing length formulation in turbulent kinetic energy (TKE) eddy-diffusivity (ED) schemes. In fact, while MYNN and MYJ have similar TKE formulations and differ only with their mixing length expressions, the BL deepening produced in these two schemes are significantly different (BL heights are about 300 m lower in the case of MYJ). Thus, one potential pathway for BL height improvement would be to develop a mixing length formulation that promotes slightly further deepening than MYNN. The key role of the mixing length has already been recognized (e.g. Mellor and Yamada 1982) and new mixing length formulations that lead to deeper boundary layers have been proposed (e.g. Teixeira and Cheinet 2004).

On the other hand some processes not explicitly represented in TKE ED schemes could be the reason for the lack of BL deepening in these schemes. For instance, non-local mixing is a potential contributor to BL deepening and is not represented explicitly in TKE ED schemes. First order

ED schemes such as YSU and ACM2 have a representation for non-local mixing (with counter-gradient terms). However, these schemes are not as successful as MYNN since they reduce BL height by about 100 m in our experiments. Siebesma et al. (2007) have shown that ED schemes that use a counter-gradient term to represent non-local mixing, significantly reduce entrainment (and BL growth) because of the way they are formulated. To overcome this issue, a physically based way of representing non-local mixing in the boundary layer has been proposed where ED and the mass-flux (MF) approximations are combined in an optimal manner. In this Eddy-Diffusivity/Mass-Flux (EDMF) approach, the ED component represents small-scale turbulence, while the larger plumes responsible for the non-local transport are represented by the MF term. This approach was originally formulated by Siebesma (2000). EDMF has been implemented in WRF by Angevine et al. (2010) and was shown to perform well for various cloudy boundary layer regimes in the single column model framework (Huang et al. 2013). However our preliminary tests in the 3D framework have not been particularly successful in reproducing the stratocumulus deck during VOCALS-REx.

The use of a shallow cumulus parameterization is another possible pathway as such parameterizations are meant to represent BL non-local moist mixing. Our tests using the CU Tiedtke parameterization confirm that the shallow cumulus mixing promotes BL deepening, though the deepening is too pronounced during VOCALS-REx. The BL height overestimation remains relatively close to observations when Tiedtke is combined with YSU, and this contributes to the realism of this simulation. When MYNN and Tiedtke are combined, the BL height is much greater than observed by about 200 m, contributing to a significant drying of the BL. As a result, the model seems to deviate towards a slightly different regime, with fewer clouds and a peak cloud region moving further offshore than observations (Fig. 1k). This highlights that the blending of the boundary layer parameterization with the cumulus parameterization is a key problem in cloudy boundary layer model development. In this context, the EDMF parameterization provides an optimal solution since it is a unified approach that combines the boundary layer and cumulus parameterizations into one single scheme (e.g. Soares et al. 2004; Suselj et al. 2013). Other methods, such as the assumed probability density function method of Golaz et al. (2002), have also been recently attempted to unify the parameterizations of boundary layer and shallow convection mixing.

Finally, another potential missing piece in all our experiments may be an explicit representation of the turbulent mixing generated by a thin layer of radiative cooling at the cloud top (e.g. Bretherton and Park 2009) (Note that this term may be particularly important for configurations with lower vertical resolution than ours). The BL scheme developed by Bretherton and Park (2009) that includes this additional term has recently been implemented in WRF. However, our preliminary tests using this scheme have not been very successful in reproducing the stratocumulus deck in the southeast Pacific.

Appendix: MP, BL and CU parameterizations

MP schemes handle phase changes of water. In this study, we test 3 MP schemes that predict the concentrations of 6 water species: water vapor, cloud liquid water, rain, snow, ice, and graupel. Two of the MP schemes, Lin et al. (1983) and WSM6 (Hong and Lim 2006), are single moment schemes. The third one, the Thompson et al. (2008) MP, is a double-moment scheme. There are many differences between these three schemes. As stratocumuli are liquid clouds, we focus here on one difference involving the liquid phase. In Lin and WSM6, the auto conversion rate from cloud liquid water to rain can be expressed as:

$$P_{aut} = \beta h(q_c - q_{co}) \tag{1}$$

where h is the Heaviside unit step function, q_c is the cloud liquid water content, q_{co} a critical water content threshold, and β the conversion rate efficiency. While β and q_{co} are kept constant in Lin, these parameters are predicted with a physically-based formula in WSM6 (Hong et al. 2003). To compute them, a critical droplet number concentration N_c is introduced, representing the concentration when cloud droplets start to coalesce in raindrops. In Thompson, the auto conversion scheme is more elaborated, but a critical droplet number concentration also plays an essential role. N_c is set to a default value of 300 cm^{-3} in WSM6 and 100 cm^{-3} in Thompson. We keep these default values in most experiments. To study the sensitivity to N_c, we also perform one additional experiment with N_c tuned to 100 cm^{-3} in WSM6.

Five different BL schemes are tested in this study. These schemes parameterize subgrid-scale turbulent vertical fluxes from prognostic grid-scale variables with an eddy-diffusivity (ED) model:

$$\overline{w'a'} = -K_a \frac{\partial \bar{a}}{\partial z} \tag{2}$$

here, a represents the variable being considered (u, v, θ or q) and K_a the eddy-diffusivity. Two different approaches are

used to compute the eddy diffusivity in the tested schemes. The first involves a first order closure and is used by YSU (Hong et al. 2006) and ACM2 (Pleim 2007). In these schemes, BL height is first diagnosed using critical Richardson theory and the eddy-diffusivity profile in the BL is then deduced. In addition to the eddy-diffusivity model, YSU and ACM2 also represent non-local mixing. There is also a representation of entrainment in YSU, which is computed as a function of surface fluxes. In the second approach, turbulent kinetic energy (TKE) closures are involved. This approach is used by MYJ (Janjic 1990), MYNN (Nakanishi and Niino 2004), and QNSE (Sukoriansky et al. 2005). In these schemes, prognostic equations are implemented to compute the TKE in any grid cell, and then the eddy diffusivity is deduced locally from mixing length theory:

$$K_a = l_m \sqrt{TKE} S_a \qquad (3)$$

here l_m is the mixing length, and S_a is a dimensionless stability function. MYNN and MYJ employ the same equations to compute TKE. However they differ in their mixing length formulation. QNSE uses different formulations for both TKE and mixing length, and is especially designed for stable stratification regimes. Non-local mixing is not represented in TKE schemes and entrainment is only implicit.

CU schemes estimate the redistribution of heat, moisture and momentum in the vertical due to convective processes. In this work, we mostly use the Kain and Fritsch (KF, 1990) scheme. This scheme only parameterizes deep convection (i.e. updrafts deeper than 2 km), and therefore does not affect boundary layer mixing. Some CU schemes also have a shallow cumulus parameterization to represent non-local transport in the boundary layer (i.e. updrafts below 2 km). To study the effect of such schemes, we present in this work a few tests with the Tiedtke scheme (Zhang et al. 2011) that includes a shallow cumulus parameterization.

References

Angevine WM, Jiang H, Mauritsen T (2010) Performance of an eddy diffusivity-mass flux scheme for shallow cumulus boundary layers. Mon Weather Rev 138(7):2895–2912

Beljaars ACM (1994) The parameterization of surface fluxes in large-scale models under free convection. Quart J R Meteor Soc 121:255–270

Borg LA, Bennartz R (2007) Vertical structure of stratiform marine boundary layer clouds and its impact on cloud albedo. Geophys Res Lett 34:L05807. doi:10.1029/2006GL028713

Bretherton CS, Park S (2009) A new moist turbulence parameterization in the community atmosphere model. J Clim 22:3422–3448

Bretherton CS, Wood R, George RC, Leon D, Allen G, Zheng X (2010) Southeast Pacific stratocumulus clouds, precipitation and boundary layer structure sampled along 20°S during VOCALS-Rex. Atmos Chem Phys 10:10639–10654

Chen F, Dudhia J (2001) Coupling an advanced land-surface hydrology model with the Penn State NCAR MM5 modeling system. Part I: model description and implementation. Mon Weather Rev 129:569–585

de Szoeke SP, Fairall CW, Wolfe DE, Bariteau L, Zuidema P (2010) Surface flux observations on the southeastern tropical pacific ocean and attribution of SST errors in coupled ocean-atmosphere models. J Clim 23:4152–4174

Dudhia J (1989) Numerical study of convection observed during the winter monsoon experiment using a mesoscale two-dimensional model. J Atmos Sci 46:3077–3107

Garreaud RD, Munoz RC (2005) The low-level jet off the sub-tropical west coast of South America: structure and variability. Mon Weather Rev 133:2246–2261

Golaz J, Larson V, Cotton W (2002) A PDF-based model for boundary layer clouds. Part I: method and model description. J Atmos Sci 59(24):3540–3551

Hong S-Y, Lim J-OJ (2006) The WRF single-moment 6-class microphysics scheme (WSM6). J Korean Meteor. Soc. 42:129–151

Hong S-Y, Dudhia J, Chen S-Y (2003) A revised approach to ice microphysical processes for bulk parameterization of clouds and precipitation. Mon Weather Rev 132:103–120

Hong S-Y, Noh Y, Dudhia J (2006) A new vertical diffusion package with an explicit treatment of entrainment processes. Mon Weather Rev 134:2318–2341

Huang H-Y, Hall A, Teixeira J (2013) Evaluation of the WRF PBL parameterizations for marine boundary layer clouds: cumulus and stratocumulus. Mon Weather Rev 141:2265–2271

Janjic ZA (1990) The step-mountain coordinate: physics package. Mon Weather Rev 118:1429–1443

Janjic ZI (1994) The step-mountain Eta coordinate model: further developments of the convection, viscous sublayer and turbulence closure schemes. Mon Weather Rev 122:927–945

Kain JS, Fritsch JM (1990) A one-dimensional entraining detraining plume model and its application in convective parameterization. J Atmos Sci 47:2784–2802

Klein SA, Hartmann DL (1993) The seasonal cycle of low stratiform clouds. J Clim 6:1587–1606

Lin Y-L, Farley RD, Orville HD (1983) Bulk parameterization of the snow field in a cloud model. J Clim Appl Meteor 22:1065–1092

Marchand R, Ackerman T, Smyth M, Rossow WB (2010) A review of cloud top height and optical depth histograms from MISR, ISCCP, and MODIS. J Geophys Res 115:D16206. doi:10.1029/2009JD013422

Mellor GL, Yamada T (1982) Development of a turbulence closure model for geophysical fluid problems. Rev Geophys Space Phys 20:851–875

Mlawer EJ, Taubman SJ, Brown PD, Iacono MJ, Clough SA (1997) Radiative transfer for inhomogeneous atmosphere: RRTM, a validated correlated-k model for the long-wave. J Geophys Res 102(D14):16663–16682

Nakanishi M, Niino H (2004) An improved Mellor-Yamada level-3 model with condensation physics: its design and verification. Bound-Layer Meteor 112:1–31

Nam C, Bony S, Dufresne J-L, Chepfer H (2012) The 'too few, too bright' tropical low-cloud problem in CMIP5 models. Geophys Res Lett 39:L21801. doi:10.1029/2012GL053421

Painemal D, Zuidema P (2011) Assessment of MODIS cloud effective radius and optical thickness retrievals over the southeast Pacific with VOCALS-Rex in situ measurements. J Geophys Res 116:D24206. doi:10.1029/2011JD016155

Platnick S, King MD (2007) Update on the MODIS collection 5 processing cloud optical and microphysical algorithm and product validation, in fourier transform spectroscopy/hyperspectral imaging and sounding of the environment, OSA Tech. Digest Ser Pap HTuA1 [CD-ROM], Opt Soc Am, Washington, DC

Platnick S, King MD, Ackerman SA, Menzel WP, Baum BA, Riedl C, Frey RA (2003) The MODIS cloud products: algorithms and examples from Terra. IEEE Trans Geosci Remote Sens 41:459–473

Pleim JE (2007) A combined local and nonlocal closure model for the atmospheric boundary layer. Part II: application and evaluation in a mesoscale meteorological model. J Appl Meteorol Clim 46:1396–1409

Rahn DA, Garreaud R (2010a) Marine boundary layer over the subtropical southeast Pacific during VOCALS-REx—Part 1: mean structure and diurnal cycle. Atmos Chem Phys 10:4491–4506

Rahn DA, Garreaud R (2010b) Marine boundary layer over the subtropical southeast Pacific during VOCALS-REx—Part 2: synoptic variability. Atmos Chem Phys 10:4507–4519

Reynolds RW, Smith TM (1994) Improved global sea surface temperature analyses. J Clim 7:929–948

Siebesma AP, J Teixeira (2000) An advection–diffusion scheme for the convective boundary layer: description and 1D results. In: Proceedings of AMS 14th symposium, boundary layers and turbulence, 133–136

Siebesma AP, Soares PMM, Teixeira J (2007) A combined eddy-diffusivity mass-flux approach for the convective boundary layer. J Atmos Sci 64:1230–1248

Skamarock WC, Klemp JB, Dudhia J, Gill DO, Barker DM, Duda MG, Huang X-Y, Wang W, Powers JG (2008) A description of the advanced research WRF version 3. NCAR Tech. Note NCAR/TN-475 + STR, p 125

Soares P, Miranda P, Siebesma AP, Teixeira J (2004) An eddy-diffusivity/mass-flux parametrization for dry and shallow cumulus convection. Quart J R Meteor Soc 130:3365–3384

Sukoriansky S, Galperin B, Perov V (2005) Application of a new spectral theory of stable stratified turbulence to the atmospheric boundary layer over sea ice. Boundary-Layer Meteorol 117:231–257

Suselj K, Teixeira J, Chung D (2013) A unified model for moist convective boundary layers based on a stochastic eddy-diffusivity/mass-flux parameterization. J Atmos Sci 70:1929–1953

Teixeira J, Cheinet S (2004) A simple mixing length formulation for the eddy-diffusivity parameterization of dry convection. Bound-Layer Meteorol 110(3):435–453

Thompson G, Field PR, Rasmussen RM, Hall WD (2008) Explicit Forecasts of winter precipitation using an improved bulk microphysics scheme. Part II: implementation of a new snow parameterization. Mon Weather Rev 136:5095–5115

Wood R, Bretherton CS, Mechoso CR, Weller RA, Huebert B, Straneo F, Albrecht BA, Coe H, Allen G, Vaughan G, Daum P, Fairall C, Chand D, Gallardo Klenner L, Garreaud R, Grados Quispe C, Covert DS, Bates TS, Krejci R, Russell LM, de Szoeke S, Brewer A, Yuter SE, Springston SR, Chaigneau A, Toniazzo T, Minnis P, Palikonda R, Abel SJ, Brown WOJ, Williams S, Fochesatto J, Brioude J (2010) The VAMOS ocean-cloud-atmosphere-land study regional experiment (VOCALS-REx): goals, platforms, and field operations. Atmos Chem Phys Discuss 10:20769–20822. doi:10.5194/acpd-10-20769-2010

Wyant MC, Wood R, Bretherton CS, Mechoso CR, Bacmeister J, Balmaseda MA, Barrett B, Codron F, Earnshaw P, Fast J, Hannay C, Kaiser JW, Kitagawa H, Klein SA, Köhler M, Manganello J, Pan H-L, Sun F, Wang S, Wang Y (2010) The PreVOCA experiment: modeling the lower troposphere in the Southeast Pacific. Atmos Chem Phys 10:4757–4774. doi:10.5194/acp-10-4757-2010

Zhang C, Wang Y, Hamilton K (2011) Improved representation of boundary layer clouds over the southeast pacific in ARW-WRF using a modified Tiedtke Cumulus parameterization scheme. Mon Weather Rev 139:3489–3513